INTERNATIONAL JOURNAL FOR NUMERICAL METHODS IN FLUIDS
Int. J. Numer. Meth. Fluids 2008; **58**:1017–1039
Published online 18 March 2008 in Wiley InterScience (www.interscience.wiley.com). DOI: 10.1002/fld.1780

Numerical experiments with several variant WENO schemes for the Euler equations

Tsang-Jen Hsieh[1], Ching-Hua Wang[1] and Jaw-Yen Yang[2,*,†]

[1]*Department of Mechanical Engineering, National Taiwan University, Taipei, Taiwan*
[2]*Institute of Applied Mechanics, National Taiwan University, Taipei, Taiwan*

SUMMARY

Numerical experiments with several variants of the original weighted essentially non-oscillatory (WENO) schemes (*J. Comput. Phys.* 1996; **126**:202–228) including anti-diffusive flux corrections, the mapped WENO scheme, and modified smoothness indicator are tested for the Euler equations. The TVD Runge–Kutta explicit time-integrating scheme is adopted for unsteady flow computations and lower–upper symmetric-Gauss–Seidel (LU-SGS) implicit method is employed for the computation of steady-state solutions. A numerical flux of the variant WENO scheme in flux limiter form is presented, which consists of first-order and high-order fluxes and allows for a more flexible choice of low-order schemes. Computations of unsteady oblique shock wave diffraction over a wedge and steady transonic flows over NACA 0012 and RAE 2822 airfoils are presented to test and compare the methods. Various aspects of the variant WENO methods including contact discontinuity sharpening and steady-state convergence rate are examined. By using the WENO scheme with anti-diffusive flux corrections, the present solutions indicate that good convergence rate can be achieved and high-order accuracy is maintained and contact discontinuities are sharpened markedly as compared with the original WENO schemes on the same meshes.

Received 28 September 2007; Revised 5 January 2008; Accepted 8 January 2008

KEY WORDS: WENO scheme; anti-diffusive flux corrections; mapped WENO scheme; contact discontinuity sharpening; transonic airfoil flow; finite volume methods; hyperbolic PDE; explicit; implicit; Euler flow; compressible flow

1. INTRODUCTION

The original design and construction of the weighted essentially non-oscillatory (WENO) schemes are based on essentially non-oscillatory (ENO) schemes, which were first introduced by Harten

*Correspondence to: Jaw-Yen Yang, Institute of Applied Mechanics, National Taiwan University, Taipei, Taiwan.
†E-mail: yangjy@spring.iam.ntu.edu.tw

Contract/grant sponsor: National Science Council; contract/grant number: NSC-95-2212-E002-055

et al. [1] in the form of cell averages. Later, Shu and Osher [2, 3] devised an efficient flux version. ENO schemes are uniformly high-order accurate right up to discontinuities, while keeping a sharp, ENO shock transition and very robust to use. ENO schemes have been applied in many different fields as Shu listed in [4]. However, they also have certain drawbacks. One main issue is that the convergence rate for the steady solution using implicit ENO scheme is generally poor. On the other hand, implicit schemes [5] as constructed out of the total variation diminishing (TVD) scheme [6] can achieve good convergence property.

The WENO schemes proposed by Liu *et al.* [7] and extended by Jiang and Shu [8] can overcome these drawbacks while keeping the robustness and high-order accuracy of ENO schemes. The concept of WENO schemes is briefly described. Instead of using only one of the candidate stencils to form the reconstruction, one uses a convex combination of all the candidate stencils. Each of the candidate stencils is assigned a weight, which determines the contribution of this stencil to the final approximation of the numerical flux. Atkins [9] also devised a version of ENO schemes using a different weighted average of stencils. A class of implicit WENO schemes has been successfully devised to solve the compressible Euler/Navier–Stokes equations [10, 11] which indicate better steady-state convergence as compared with their implicit ENO counterpart. The implicit WENO methods have also been successfully extended to incompressible flow problems [12] based on artificial compressibility formulation [13]. Good convergence rate to steady-state solution has been illustrated.

In recent years, several variants and improvements of the original WENO schemes [8] have been proposed [14–18]. By introducing an anti-diffusive flux, Despres and Lagoutiere [14] proposed a first-order approach called limited downwind scheme to prevent the smearing of contact discontinuities while keeping nonlinear stability. Later Bouchut [15] modified this scheme to satisfy entropy conditions and also gave a simple explicit formula for this limited downwind anti-diffusive flux. As inspired by these works [14, 15], Xu and Shu [16] developed an anti-diffusive flux correction technique based on high-order finite difference WENO scheme, the resulting scheme maintains high-order accuracy in smooth regions, non-oscillatory behavior near discontinuities, and sharp contact discontinuity resolution. Also, a mapped WENO scheme has been devised by Henrick *et al.* [17], which improves over the original WENO scheme at critical points. Zhang and Shu [18] suggested a modified smoothness indicator for the fifth-order WENO scheme near a steady shock region and they showed that the residue for the WENO scheme with the new smoothness indicator can converge to machine zero for one- and two-dimensional steady problems with strong shock wave when there is no influence from the boundary conditions.

In this paper, following [16–18] and [10, 11], first, the explicit TVD Runge–Kutta method is adopted for the variant WENO methods for unsteady flow calculations. Second, an implicit version of the WENO scheme with anti-diffusive flux corrections is also constructed for the two-dimensional compressible Euler equations for computing steady-state flows. The mapped WENO and original WENO with modified smoothness monitor are also considered. A new form of numerical flux for each of the variant WENO schemes is presented, which consists of first-order and high-order fluxes. Several first-order dissipative schemes can be used such as Lax–Friedrichs scheme [19], Roe's scheme [20], or the flux vector splitting schemes. In order to improve the efficiency and convergence to the steady state, the lower–upper symmetric-Gauss–Seidel (LU-SGS) implicit algorithm [21, 22] is adopted. We apply the resulting schemes to compute standard transonic flows over NACA 0012 and RAE 2822 airfoils and an oblique shock over a wedge in a shock tube to test the accuracy and the improved resolution of contact discontinuities of the methods. In *addition*, we make comparisons in the convergence property between variants of

DOI: 10.1002/fld

implicit schemes, including the original WENO scheme, the WENO scheme with anti-diffusive flux corrections, the WENO scheme with modified smoothness indicator, and the mapped WENO scheme [17].

2. GOVERNING EQUATIONS

The governing equations are the time-dependent Euler equations, which express the conservation of mass, momentum, and energy for an inviscid compressible gas. In Cartesian coordinates, the Euler equations are given by

$$\frac{\partial Q}{\partial t}+\frac{\partial E}{\partial x}+\frac{\partial F}{\partial y}=0 \tag{1}$$

with

$$Q=(\rho,\rho u,\rho v,e)^{\mathrm{T}}$$
$$E=(\rho u,\rho u^2+p,\rho uv,(e+p)u)^{\mathrm{T}}$$
$$F=(\rho v,\rho vu,\rho v^2+p,(e+p)v)^{\mathrm{T}}$$

where ρ is the density, u and v are the x and y components of the velocity, respectively, and e is the energy per unit volume. The pressure p is related to the dependent variables by the equation of state for a perfect gas:

$$p=(\gamma-1)[e-\rho(u^2+v^2)/2] \tag{2}$$

where γ is the ratio of specific heats.

To facilitate solution of the governing equations for problem with general geometry, Equation (1) is transformed into the generalized coordinates (ξ,η) as

$$\begin{gathered}\xi=\xi(x,y),\quad \eta=\eta(x,y)\\ \frac{\partial \hat{Q}}{\partial t}+\frac{\partial \hat{E}}{\partial \xi}+\frac{\partial \hat{F}}{\partial \eta}=0\end{gathered} \tag{3}$$

where

$$\hat{Q}=\frac{1}{J}Q,\quad \hat{E}=\frac{1}{J}(\xi_x E+\xi_y F),\quad \hat{F}=\frac{1}{J}(\eta_x E+\eta_y F)$$
$$\xi_x=Jy_\eta,\quad \xi_y=-Jx_\eta$$
$$\eta_x=-Jy_\xi,\quad \eta_y=Jx_\xi$$

with the Jacobian J: $J=1/(x_\xi y_\eta-x_\eta y_\xi)$.

To allow for the development of a discrete control volume formulation, Equation (3) can be presented in integral form:

$$\frac{\partial}{\partial t}\left(\frac{1}{S}\int_S Q\,\mathrm{d}S\right)+\frac{1}{S}\oint_\Omega H\cdot\mathbf{n}\,\mathrm{d}\Omega=0 \tag{4}$$

DOI: 10.1002/fld

where $H=\hat{E}n_\xi+\hat{F}n_\eta$ and S is the area of the cell that is bounded by the boundary curve Ω with the outward unit normal $\mathbf{n}$.

3. VARIANT WENO METHODS

3.1. WENO spatial discretization

A semi-discrete finite volume method is used to ensure that the final converged solution is independent of the integration procedure and to avoid metric singularity problems. The finite volume method is based on the local flux balance of each mesh cell. The semi-discrete form of Equation (4) can be expressed as

$$\left(\frac{\partial \hat{Q}}{\partial t}\right)_{i,j}=-\frac{1}{S}[(\tilde{E})_{i+1/2,j}-(\tilde{E})_{i-1/2,j}]-\frac{1}{S}[(\tilde{F})_{i,j+1/2}-(\tilde{F})_{i,j-1/2}] \tag{5}$$

where (i, j) is the control point of finite area. The spatial differencing adopts third-order ($r=2$) and fifth-order ($r=3$) weighted essentially non-oscillatory schemes (denoted as WENO3 and WENO5) [8] for the inviscid convective fluxes $(\tilde{E}, \tilde{F})$. The WENO numerical flux at a cell surface $i+1/2$ in direction i can be put into the form of a flux limiter method [10, 11] and is given by

$$\tilde{E}_{i+1/2,j}=\tilde{E}^L_{i+1/2,j}+\tilde{E}^H_{i+1/2,j} \tag{6}$$

where $\tilde{E}^L$ is the numerical flux of a first-order dissipative scheme, which includes either the Lax–Friedrichs scheme [19], the Roe scheme [20], or any other entropy-satisfying positive scheme. For the Roe scheme, we have

$$\tilde{E}^L_{i+1/2,j}=\tfrac{1}{2}[\hat{E}_{i,j}+\hat{E}_{i+1,j}-(R|\Lambda|R^{-1})_{i+1/2,j}(\hat{Q}_{i+1,j}-\hat{Q}_{i,j})] \tag{7}$$

where $\hat{E}_{i,j}$ and $\hat{E}_{i+1,j}$ are physical fluxes and R is the similarity matrix consisting of the right eigenvectors of the Euler system linearized around the Roe-averaged state between $\hat{Q}_{i+1,j}$ and $\hat{Q}_{i,j}$. For the Lax–Friedrichs scheme, one has

$$\tilde{E}^L_{i+1/2,j}=\tfrac{1}{2}[\hat{E}_{i,j}+\hat{E}_{i+1,j}-\alpha(\hat{Q}_{i+1,j}-\hat{Q}_{i,j})] \tag{8}$$

where $\alpha=\max_u|\hat{E}'(\hat{Q})|$ is a constant. The maximum is taken over the relevant range of $\hat{Q}$. $\tilde{E}^H$ is a high-order WENO flux, defined as

$$\tilde{E}^H_{i+1/2,j}=\sum_{s=1}^{4}\tilde{E}^H_{(i+1/2,j),s}\cdot r_s \tag{9}$$

For the case of WENO3 ($r=2$), the high-order numerical flux is given by

$$\begin{aligned}\tilde{E}^{H2}_{(i+1/2,j),s}=&\frac{\omega^+_{0,s}}{2}\Delta E^+_{(i-1/2,j),s}+\frac{\omega^+_{1,s}}{2}\Delta E^+_{(i+1/2,j),s}\\&-\frac{\omega^-_{0,s}}{2}\Delta E^-_{(i+1/2,j),s}-\frac{\omega^-_{1,s}}{2}\Delta E^-_{(i+3/2,j),s}\end{aligned} \tag{10}$$

DOI: 10.1002/fld

where

$$\Delta E^{\pm}_{(i+1/2,j),s} = l_s \cdot \Delta E^{\pm}_{i+1/2,j} \tag{11}$$

$$\Delta E^{+}_{i+1/2,j} = \hat{E}_{i+1,j} - \tilde{E}^{L}_{i+1/2,j} \tag{12}$$

$$\Delta E^{-}_{i+1/2,j} = \tilde{E}^{L}_{i+1/2,j} - \hat{E}_{i,j} \tag{13}$$

The weights $\omega^{\pm}$ are defined by

$$\omega^{\pm}_{k,s} = \frac{\alpha^{\pm}_{k,s}}{\alpha^{\pm}_{0,s} + \alpha^{\pm}_{1,s}}, \quad k = 0, 1 \tag{14}$$

where

$$\alpha^{+}_{0,s} = \tfrac{1}{3}(\varepsilon + \mathrm{IS}^{+}_{0,s})^{-2}, \quad \alpha^{+}_{1,s} = \tfrac{2}{3}(\varepsilon + \mathrm{IS}^{+}_{1,s})^{-2} \tag{15}$$

$$\alpha^{-}_{0,s} = \tfrac{2}{3}(\varepsilon + \mathrm{IS}^{-}_{0,s})^{-2}, \quad \alpha^{-}_{1,s} = \tfrac{1}{3}(\varepsilon + \mathrm{IS}^{-}_{1,s})^{-2} \tag{16}$$

Here $\varepsilon = 10^{-6}$ chosen to avoid the division by zero in Equations (15) and (16) and IS are the smooth indicators, defined as

$$\mathrm{IS}^{+}_{0,s} = (\Delta E^{+}_{(i-1/2,j),s})^2, \quad \mathrm{IS}^{+}_{1,s} = (\Delta E^{+}_{(i+1/2,j),s})^2 \tag{17}$$

$$\mathrm{IS}^{-}_{0,s} = (\Delta E^{-}_{(i+1/2,j),s})^2, \quad \mathrm{IS}^{-}_{1,s} = (\Delta E^{-}_{(i+3/2,j),s})^2 \tag{18}$$

In the above, r_s (column vector) and l_s (row vector) are the sth right and left eigenvectors of the Jacobian matrices, respectively.

For the case of WENO5 ($r = 3$), we have

$$\tilde{E}^{H3}_{(i+1/2,j),s} = \tfrac{1}{6}(\omega^{+}_{0,s} q^{+}_0 + \omega^{+}_{1,s} q^{+}_1 + \omega^{+}_{2,s} q^{+}_2 + \omega^{-}_{0,s} q^{-}_0 + \omega^{-}_{1,s} q^{-}_1 + \omega^{-}_{2,s} q^{-}_2) \tag{19}$$

where

$$q^{+}_0 = -2\Delta E^{+}_{(i-3/2,j),s} + 5\Delta E^{+}_{(i-1/2,j),s}, \quad q^{+}_1 = \Delta E^{+}_{(i-1/2,j),s} + 2\Delta E^{+}_{(i+1/2,j),s}$$

$$q^{+}_2 = 4\Delta E^{+}_{(i+1/2,j),s} - \Delta E^{+}_{(i+3/2,j),s}, \quad q^{-}_0 = \Delta E^{-}_{(i-1/2,j),s} - 4\Delta E^{-}_{(i+1/2,j),s}$$

$$q^{-}_1 = -2\Delta E^{-}_{(i+1/2,j),s} - \Delta E^{-}_{(i+3/2,j),s}, \quad q^{-}_2 = -5\Delta E^{-}_{(i+3/2,j),s} + 2\Delta E^{-}_{(i+5/2,j),s}$$

and the weights for stencil $\omega^{\pm}$ are

$$\omega^{\pm}_{k,s} = \frac{\alpha^{\pm}_{k,s}}{\alpha^{\pm}_{0,s} + \alpha^{\pm}_{1,s} + \alpha^{\pm}_{2.s}}, \quad k = 0, 1, 2 \tag{20}$$

DOI: 10.1002/fld

where

$$
\begin{aligned}
&\alpha^{+}_{0,s}=\tfrac{1}{10}(\varepsilon+\mathrm{IS}^{+}_{0,s})^{-2},\quad \alpha^{+}_{1,s}=\tfrac{6}{10}(\varepsilon+\mathrm{IS}^{+}_{1,s})^{-2},\quad \alpha^{+}_{2,s}=\tfrac{3}{10}(\varepsilon+\mathrm{IS}^{+}_{2,s})^{-2}\\
&\alpha^{-}_{0,s}=\tfrac{3}{10}(\varepsilon+\mathrm{IS}^{-}_{0,s})^{-2},\quad \alpha^{-}_{1,s}=\tfrac{6}{10}(\varepsilon+\mathrm{IS}^{-}_{1,s})^{-2},\quad \alpha^{-}_{2,s}=\tfrac{1}{10}(\varepsilon+\mathrm{IS}^{-}_{2,s})^{-2}\\
&\mathrm{IS}^{+}_{0,s}=\tfrac{13}{12}(-\Delta E^{+}_{(i-3/2,j),s}+\Delta E^{+}_{(i-1/2,j),s})^2+\tfrac{1}{4}(-\Delta E^{+}_{(i-3/2,j),s}+3\Delta E^{+}_{(i-1/2,j),s})^2\\
&\mathrm{IS}^{+}_{1,s}=\tfrac{13}{12}(-\Delta E^{+}_{(i-1/2,j),s}+\Delta E^{+}_{(i+1/2,j),s})^2+\tfrac{1}{4}(-\Delta E^{+}_{(i-1/2,j),s}-\Delta E^{+}_{(i+1/2,j),s})^2\\
&\mathrm{IS}^{+}_{2,s}=\tfrac{13}{12}(-\Delta E^{+}_{(i+1/2,j),s}+\Delta E^{+}_{(i+3/2,j),s})^2+\tfrac{1}{4}(-3\Delta E^{+}_{(i+1/2,j),s}+\Delta E^{+}_{(i+3/2,j),s})^2\\
&\mathrm{IS}^{-}_{0,s}=\tfrac{13}{12}(-\Delta E^{-}_{(i-1/2,j),s}+\Delta E^{-}_{(i+1/2,j),s})^2+\tfrac{1}{4}(-\Delta E^{-}_{(i-1/2,j),s}+3\Delta E^{-}_{(i+1/2,j),s})^2\\
&\mathrm{IS}^{-}_{1,s}=\tfrac{13}{12}(-\Delta E^{-}_{(i+1/2,j),s}+\Delta E^{-}_{(i+3/2,j),s})^2+\tfrac{1}{4}(-\Delta E^{-}_{(i+1/2,j),s}-3\Delta E^{-}_{(i+3/2,j),s})^2\\
&\mathrm{IS}^{-}_{2,s}=\tfrac{13}{12}(-\Delta E^{-}_{(i+3/2,j),s}+\Delta E^{-}_{(i+5/2,j),s})^2+\tfrac{1}{4}(-3\Delta E^{-}_{(i+3/2,j),s}+\Delta E^{-}_{(i+5/2,j),s})^2
\end{aligned}
\tag{21}
$$

3.2. Anti-diffusive flux corrections for WENO schemes

The purpose of the anti-diffusive flux corrections is to improve the resolution of contact discontinuities without sacrificing accuracy and stability of the original WENO scheme. Consider an anti-diffusive flux in the following form [16]:

$$
\tilde{E}^{a}_{i+1/2,j}=\tilde{E}^{-}_{i+1/2,j}+\varphi_i\cdot\min\ \mathrm{mod}\left(\frac{\hat{E}_{i,j}-\hat{E}_{i-1,j}}{\eta}+\tilde{E}^{-}_{i-1/2,j}-\tilde{E}^{-}_{i+1/2,j},\tilde{E}^{+}_{i+1/2,j}-\tilde{E}^{-}_{i+1/2,j}\right)
\tag{22}
$$

where $\eta=\Delta t/\Delta x$ is the CFL number and φ_i is the discontinuity indicator with its value between 0 and 1 and is defined by

$$
\varphi_i=\frac{\beta_i}{\beta_i+\gamma_i}
$$

where

$$
\beta_i=\left(\frac{\alpha_i}{\alpha_i-1}+\frac{\alpha_{i+1}}{\alpha_{i+2}}\right)^2,\quad \gamma_i=\frac{|\hat{E}_{i\,\max}-\hat{E}_{i\,\min}|^2}{\alpha_i},\quad \alpha_i=(|\hat{E}_{i-1}-\hat{E}_i|+\varsigma)^2
$$

with ς being a small positive number taken as 10^{-6}.

3.3. A modified smoothness indicator of WENO scheme

The nonlinear weights and the smoothness indicator play a significant role in the resolution near shock region, and they have a direct relationship to the post-shock oscillation as well as to convergence property. The original smoothness indicator in smooth region in Jiang and Shu [8]

DOI: 10.1002/fld

can be expressed as follows:

$$\begin{aligned}
\mathrm{IS}_0^+ &= \tfrac{13}{12}(f_{i-2}^+ - 2f_{i-1}^+ + f_i^+)^2 + \tfrac{1}{4}(f_{i-2}^+ - 4f_{i-1}^+ + 3f_i^+)^2 \\
\mathrm{IS}_1^+ &= \tfrac{13}{12}(f_{i-1}^+ - 2f_i^+ + f_{i+1}^+)^2 + \tfrac{1}{4}(f_{i-1}^+ - f_{i+1}^+)^2 \\
\mathrm{IS}_2^+ &= \tfrac{13}{12}(f_i^+ - 2f_{i+1}^+ + f_{i+2}^+)^2 + \tfrac{1}{4}(3f_i^+ - 4f_{i+1}^+ + f_{i+2}^+)^2 \\
\mathrm{IS}_0^- &= \tfrac{13}{12}(f_{i-1}^- - 2f_i^- + f_{i+1}^-)^2 + \tfrac{1}{4}(f_{i-1}^- - 4f_i^- + 3f_{i+1}^-)^2 \\
\mathrm{IS}_1^- &= \tfrac{13}{12}(f_i^- - 2f_{i+1}^- + f_{i+2}^-)^2 + \tfrac{1}{4}(f_i^- - 3f_{i+2}^-)^2 \\
\mathrm{IS}_2^- &= \tfrac{13}{12}(f_{i+1}^- - 2f_{i+2}^- + f_{i+3}^-)^2 + \tfrac{1}{4}(3f_{i+1}^- - 4f_{i+2}^- + f_{i+3}^-)^2
\end{aligned} \tag{23}$$

Zhang and Shu [18] suggested a modified smoothness indicator for the fifth-order WENO scheme near a steady shock region:

$$\begin{aligned}
\mathrm{IS}_0^+ &= (f_{i-2}^+ - 4f_{i-1}^+ + 3f_i^+)^2 \\
\mathrm{IS}_1^+ &= (f_{i-1}^+ - f_{i+1}^+)^2 \\
\mathrm{IS}_2^+ &= (3f_i^+ - 4f_{i+1}^+ + f_{i+2}^+)^2 \\
\mathrm{IS}_0^- &= (f_{i-1}^- - 4f_i^- + 3f_{i+1}^-)^2 \\
\mathrm{IS}_1^- &= (f_i^- - 3f_{i+2}^-)^2 \\
\mathrm{IS}_2^- &= (3f_{i+1}^- - 4f_{i+2}^- + f_{i+3}^-)^2
\end{aligned} \tag{24}$$

In this paper, we rewrite these modified smoothness indicators in the form similar to Equation (21) as follows:

$$\begin{aligned}
\mathrm{IS}_{0,s}^+ &= (-\Delta E_{(i-3/2,j),s}^+ + 3\Delta E_{(i-1/2,j),s}^+)^2 \\
\mathrm{IS}_{1,s}^+ &= (-\Delta E_{(i-1/2,j),s}^+ - \Delta E_{(i+1/2,j),s}^+)^2 \\
\mathrm{IS}_{2,s}^+ &= (-3\Delta E_{(i+1/2,j),s}^+ + \Delta E_{(i+3/2,j),s}^+)^2 \\
\mathrm{IS}_{0,s}^- &= (-\Delta E_{(i-1/2,j),s}^- + 3\Delta E_{(i+1/2,j),s}^-)^2 \\
\mathrm{IS}_{1,s}^- &= (-\Delta E_{(i+1/2,j),s}^- - 3\Delta E_{(i+3/2,j),s}^-)^2 \\
\mathrm{IS}_{2,s}^- &= (-3\Delta E_{(i+3/2,j),s}^- + \Delta E_{(i+5/2,j),s}^-)^2
\end{aligned} \tag{25}$$

3.4. Mapped WENO schemes

Henrich *et al.* [17] observed that the nonlinear weights with the smoothness indicator given by Equation (23) may lose accuracy at certain critical points and they introduced a new mapped function for the fifth-order WENO ($r=3$) scheme as follows:

$$g_r(\omega) = \frac{\omega(\omega_r^0 + (\omega_r^0)^2 - 3\omega_r^0\omega + \omega^2)}{(\omega_r^0)^2 + (1-2\omega_r^0)\omega}, \quad r=0,1,2 \tag{26}$$

where $\omega \in [0,1]$ and $\omega_0^0 = 0.1$, $\omega_1^0 = 0.6$, and $\omega_2^0 = 0.3$ are the optimal weights.

DOI: 10.1002/fld

This function is monotonically increasing with a finite slope and has the following features:

$$g_r(0)=0, \quad g_r(1)=1, \quad g_r(\omega_r^0)=\omega_r^0, \quad g_r'(\omega_r^0)=0 \quad \text{and} \quad g_r''(\omega_r^0)=0$$

An approximation of weights is given by

$$\omega_r^* = g_r(\omega_r) \tag{27}$$

where ω_r are computed by Equation (20). The mapped weights are defined according to

$$\omega_r^{\mathrm{M}} = \frac{\omega_r^*}{\sum_{i=0}^{2} \omega_i^*} \tag{28}$$

This mapped WENO scheme has shown that it can improve accuracy at smooth extreme [17]. It was also found that the small number ε, used in the original WENO scheme to avoid the division by zero, is related to the convergence rate to steady state.

An additional advantage is that accuracy depends much less on the magnitude of the parameter ε and hence it can be taken close to machine zero.

4. EXPLICIT AND IMPLICIT TIME DISCRETIZATION

4.1. Explicit third-order TVD Runge–Kutta time discretization

After the spatial derivatives are discretized with the variant WENO schemes, a set of ordinary differential equations can be obtained:

$$\frac{\mathrm{d}u}{\mathrm{d}t} = L(u) \tag{29}$$

The operator has the following form:

$$L(u) = -\frac{1}{\Delta x}[\hat{F}_{j+1/2} - \hat{F}_{j-1/2}] \tag{30}$$

This set of ordinary differential equations can be discretized by the modified third-order TVD Runge–Kutta method [16] as follows:

$$\begin{aligned} u^{(1)} &= u^n + \Delta t\, L(u^n) \\ u^{(2)} &= u^n + \tfrac{1}{4}\Delta t\, L'(u^n) + \tfrac{1}{4}\Delta t\, L(u^{(1)}) \\ u^{(n+1)} &= u^n + \tfrac{1}{6}\Delta t\, L''(u^n) + \tfrac{1}{6}\Delta t\, L(u^n) + \tfrac{2}{3}\Delta t\, L(u^{(2)}) \end{aligned} \tag{31}$$

where the operators L, L' and L'' are defined, respectively, by

$$\begin{aligned} L(u^n) &= -\lambda_{i,j}(\hat{f}^a_{i+1/2,j} - \hat{f}^a_{i-1/2,j}) \\ L'(u^n) &= -\lambda_{i,j}(\bar{f}^a_{i+1/2,j} - \bar{f}^a_{i-1/2,j}) \\ L''(u^n) &= -\lambda_{i,j}(\tilde{f}^a_{i+1/2,j} - \tilde{f}^a_{i-1/2,j}) \end{aligned} \tag{32}$$

DOI: 10.1002/fld

The anti-diffusive fluxes in Equation (32) are defined, respectively, by

$$\hat{f}^a_{i+1/2,j} = \hat{f}^-_{i+1/2,j} + \min\text{ mod}\left(\frac{u_{i,j}-u_{i-1,j}}{2\lambda_{i,j}} + \hat{f}^-_{i-1/2,j} - \hat{f}^-_{i+1/2,j}, \hat{f}^+_{i+1/2,j} - \hat{f}^-_{i+1/2,j}\right)$$

$$\bar{f}^a_{i+1/2,j} = \begin{cases} \hat{f}^-_{i+1/2,j} + \min\text{ mod}\left(\dfrac{4(u_{i,j}-u_{i-1,j})}{2\lambda_{i,j}}\right. \\ \quad \left. + \hat{f}^-_{i-1/2,j} - \hat{f}^-_{i+1/2,j}, \hat{f}^+_{i+1/2,j} - \hat{f}^-_{i+1/2,j}\right), & bc>0,\ \ |b|<|c| \\ \hat{f}^a_{i+1/2,j} & \text{otherwise} \end{cases} \tag{33}$$

$$\tilde{f}^a_{i+1/2,j} = \begin{cases} \hat{f}^-_{i+1/2,j} + \min\text{ mod}\left(\dfrac{6(u_{i,j}-u_{i-1,j})}{2\lambda_{i,j}}\right. \\ \quad \left. + \hat{f}^-_{i-1/2,j} - \hat{f}^-_{i+1/2,j}, \hat{f}^+_{i+1/2,j} - \hat{f}^-_{i+1/2,j}\right), & bc>0,\ \ |b|<|c| \\ \hat{f}^a_{i+1/2,j} & \text{otherwise} \end{cases}$$

where $b = u_{i,j} - u_{i-1,j}/2\lambda_{i,j} + \hat{f}^-_{i-1/2,j} - \hat{f}^-_{i+1/2,j}, c = \hat{f}^+_{i+1/2,j} - \hat{f}^-_{i+1/2,j}$ and $\lambda_{i,j} = \Delta t/\Delta x$.

4.2. LU-SGS implicit methods

An unfactored implicit scheme can be obtained for Equation (5) from a nonlinear implicit scheme by linearizing the flux vectors about the previous time step and dropping terms of second and higher orders:

$$\left[\frac{S}{\Delta t}I + (\delta_\xi \hat{A} + \delta_\eta \hat{B})\right]\Delta\hat{Q}_{i,j} = -[(\tilde{E})^n_{i+1/2,j} - (\tilde{E})^n_{i-1/2,j}] - [(\tilde{F})^n_{i,j+1/2} - (\tilde{F})^n_{i,j-1/2}]$$
$$\equiv \text{RHS} \tag{34}$$

where I is the identity matrix and n is the time level, δ_ξ, δ_η are the difference operators, $\hat{A}, \hat{B}$ are the Jacobian matrices of inviscid fluxes, and $\Delta\hat{Q} = \hat{Q}^{n+1} - \hat{Q}^n$ is the increment of conservative variables. Yoon and Jameson [21] and Jameson and Yoon [22] developed a lower–upper (LU) factored implicit scheme that is unconditionally stable in any number of space dimensions. Applying the LU factorization to Equation (34), the following LU scheme is obtained:

$$\left[\frac{S}{\Delta t}I + (\delta^-_\xi \hat{A}^+ + \delta^-_\eta \hat{B}^+)\right]\left[\frac{S}{\Delta t}I + (\delta^+_\xi \hat{A}^- + \delta^+_\eta \hat{B}^-)\right]\Delta\hat{Q} = \text{RHS} \tag{35}$$

where $\delta^-_\xi, \delta^-_\eta$ are backward difference operators and $\delta^+_\xi, \delta^+_\eta$ are forward difference operators. The split Jacobian matrices of the flux vectors are constructed so that the eigenvalues of '+' matrices are non-negative and those of '−' matrices are non-positive, i.e.

$$\hat{A}^\pm = R_\xi \Lambda^\pm_\xi R^{-1}_\xi, \quad \hat{B}^\pm = R_\eta \Lambda^\pm_\eta R^{-1}_\eta$$

where R_ξ and R^{-1}_ξ are similarity transformation matrices of the eigenvectors of $\hat{A}$.

DOI: 10.1002/fld

The LU-SGS implicit factorization scheme of Yoon and Jameson [21] and Jameson and Yoon [22] for Equation (34), using the above relations, can be derived by combining the advantages of LU factorization and SGS relaxation. The LU-SGS scheme can be expressed as

$$LD^{-1}U\Delta\hat{Q}=\text{RHS} \tag{36}$$

where

$$L=\frac{S}{\Delta t}I+(\delta_{\xi}^{-}\hat{A}^{+}+\delta_{\eta}^{-}\hat{B}^{+}-\hat{A}^{-}-\hat{B}^{-})$$

$$D=\frac{S}{\Delta t}I+(\hat{A}^{+}-\hat{A}^{-}+\hat{B}^{+}-\hat{B}^{-})$$

$$U=\frac{S}{\Delta t}I+(\delta_{\xi}^{+}\hat{A}^{-}+\delta_{\eta}^{+}\hat{B}^{-}+\hat{A}^{+}+\hat{B}^{+})$$

Equation (36) can be inverted in three steps

$$\begin{aligned}\Delta\hat{Q}^{*}&=L^{-1}\text{RHS}\\ \Delta\hat{Q}^{**}&=D\hat{Q}^{*}\\ \Delta\hat{Q}&=U^{-1}\hat{Q}^{**}\end{aligned} \tag{37}$$

It is interesting to note that the present implicit algorithm (LU-SGS) is completely vectorizable on $i+j=$constant oblique lines of sweep.

It is noted that the RHS defined by Equation (34) can be evaluated using either the original WENO method, flux corrected WENO method, WENO with modified smoothness indicator or the mapped WENO method. Our numerical experiments are based on these variants of WENO methods and their respective features are examined.

5. BOUNDARY CONDITIONS

The boundary condition imposed on the solid surface is the tangency condition for inviscid flows. The curvature-corrected symmetry technique [23] is applied. For the grid sketched in Figure 1, we locate two image cells below the surface, outside the computational domain. The pressures at the image points are given by

$$p_{-1}=p_1-\rho_1\frac{\tilde{u}_1^2}{r}\Delta n_1 \tag{38}$$

$$p_{-2}=p_2-\rho_1\frac{\tilde{u}_1^2}{r}\Delta n_2 \tag{39}$$

where $\tilde{u}$ is the component of the velocity tangent to the surface, r is the surface curvature, Δn_1 represents the distance between cell center 1 and the image-cell center -1, and likewise Δn_2 is the distance between 2 and -2.

DOI: 10.1002/fld

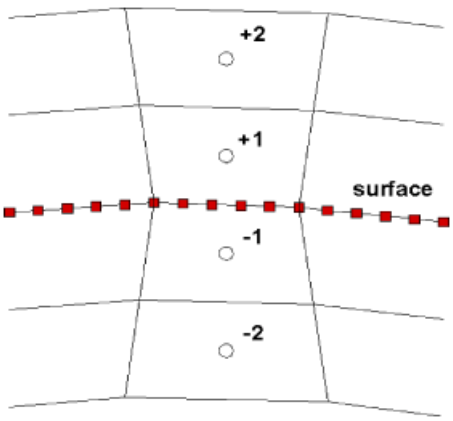

Figure 1. Image cells for curvature-corrected symmetry technique.

The other flow quantities may be evaluated by assuming symmetric values of the entropy and total enthalpy:

$$\rho_{-1}=\rho_1\left(\frac{p_{-1}}{p_1}\right)^{1/\gamma},\quad \rho_{-2}=\rho_2\left(\frac{p_{-2}}{p_2}\right)^{1/\gamma}$$

and

$$\tilde{u}_{-1}^2=\tilde{u}_1^2+\frac{2\gamma}{\gamma-1}\left(\frac{p_1}{\rho_1}-\frac{p_{-1}}{\rho_{-1}}\right)+\tilde{v}_1^2-v_{-1}^2$$

$$\tilde{u}_{-2}^2=\tilde{u}_2^2+\frac{2\gamma}{\gamma-1}\left(\frac{p_2}{\rho_2}-\frac{p_{-2}}{\rho_{-2}}\right)+\tilde{v}_2^2-v_{-2}^2$$

where $\tilde{v}$ is the component of the velocity normal to the surface and is given by

$$\tilde{v}_{-1}=\tilde{v}_1$$

$$\tilde{v}_{-2}=3\tilde{v}_{-1}+2\left[\tilde{v}_1+\frac{\tilde{v}_1-\tilde{v}_2}{2}\right]\left(\frac{\rho_1+(\rho_1-\rho_2)/2}{\rho_{-1}+(\rho_{-1}-\rho_{-2})/2}\right)^{1/2}$$

$$p_w=\left[p_1\Delta n_2^2-p_2\Delta n_1^2-\rho_1\frac{\tilde{u}_1^2}{2r}\Delta n_1\Delta n_2(\Delta n_2-\Delta n_1)\right]\Big/(\Delta n_2^2-\Delta_1^2)$$

where p_w is the value of surface pressure. In the far field, we also locate two image cells outside the computational domain. All the flow quantities at those cells are fixed to freestream conditions.

6. RESULTS AND DISCUSSION

Presented here are the results of three two-dimensional inviscid compressible flow problems to illustrate the explicit and implicit variant WENO schemes. These are unsteady oblique shock wave

DOI: 10.1002/fld

diffraction over a wedge in a shock tube, steady transonic flow over an NACA 0012 airfoil, and steady transonic flow over an RAE 2822 airfoil. Our main purpose is to illustrate the accuracy of variant WENO methods and contact discontinuities' sharpening and shock-capturing capability of the proposed schemes as well as the convergence property of the implicit WENO methods with anti-diffusive flux corrections. Four schemes, denoted as WENO schemes, the WENO scheme with anti-diffusive flux corrections, the mapped WENO scheme with anti-diffusive flux corrections, and finally the WENO scheme with both anti-diffusive flux corrections and modified smoothness indicator, have been tested. Here the WENO5-R means that the original fifth-order WENO scheme with $r=3$ is used and containing Roe's flux as the low-order flux, whereas the WENO5-LF contains Lax Friedrich's flux as the low-order flux. It is noted that when Roe's first-order method was used as the low-order flux, a Harten-type entropy fix with $\delta=0.1$ [6] was used in all the following results.

6.1. Unsteady oblique shock wave diffractions by a wedge with experimental comparisons

The propagation and diffraction of shock waves past solid bodies have received considerable attention in the past, both experimentally and computationally. Studies by Schardin [24] employed high-speed cinematography and the detailed sequence of a shock wave impinging on a wedge in a shock tube was examined. The result was a series of shadowgraphs taken at 13.6 μs intervals which clearly showed the diffraction of a Mach 1.3 shock as it passed the wedge and the resulting vortex on the back face of the wedge, as well as shock/vortex interactions. This study provided a high-quality experimental basis for the present computational work.

In order to compare with the flow visualization experiment by Schardin [24], our study examines, through the WENO5-R with anti-diffusive flux corrections scheme, the two-dimensional, unsteady problem of a Mach 1.3 shock wave impinging on a 55° wedge. Boundary conditions consists of fixed quantities of density, momentum, and energy for the inflow conditions; tangent velocity vectors along the wedge surface, plane of symmetry, and the upper wall; and free outflow boundary conditions. The numerical domain shown in Figure 2 is intended to simulate the upper half of the symmetric flowfield of Schardin. There are two grid systems used for comparison; the coarse grid consists of two blocks with 129×125 and 207×217 cells, and the fine grid consists of two blocks with 255×185 and 311×325 cells

First, a series of density gradient contours at different instants are shown in Figure 3 to depict the complex unsteady shock diffraction process. Frame 4, one of the sequent frames in Schardin's experiment, is shown in the lower half of Figure 4, which corresponds to our numerical result

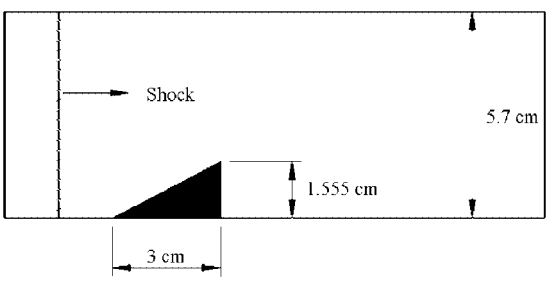

Figure 2. The computational domain simulating the upper half of the symmetric flowfield of Schardin.

DOI: 10.1002/fld

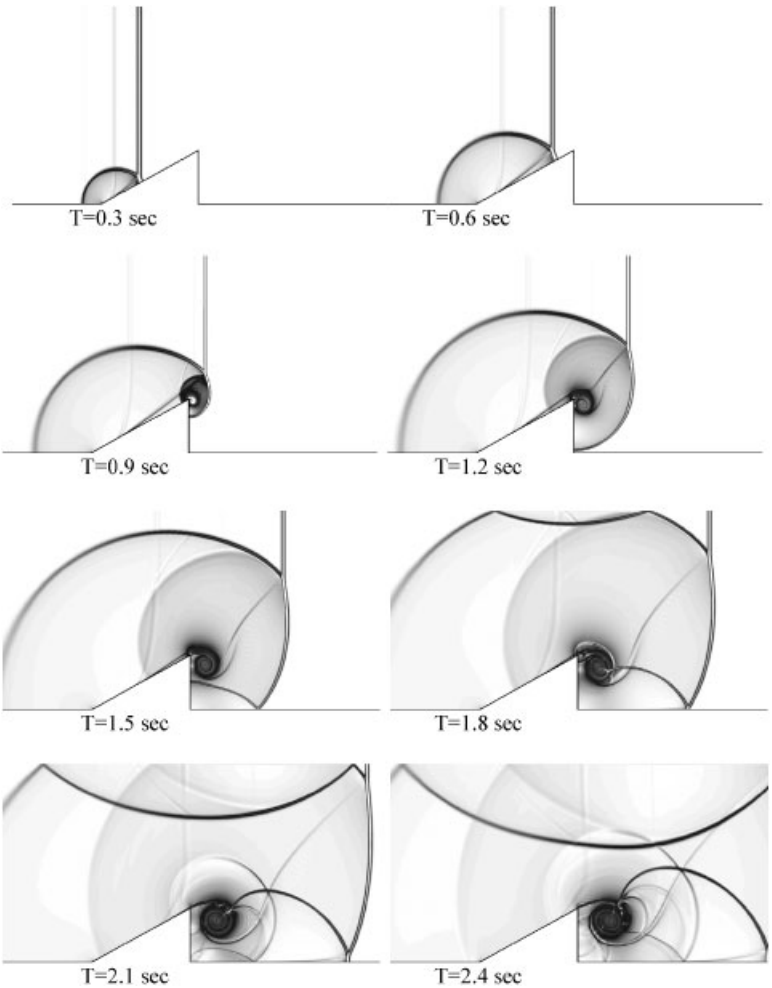

Figure 3. A series of $\nabla\rho$ contours at different instants using the WENO5_R scheme.

of $\nabla\rho$ contours using WENO5_R with anti-diffusive flux corrections scheme and the fine grid system. A later stage of the diffraction, corresponding to frame 11, is depicted in Figure 5 together with the experimental picture. The initial reflected shock (B) has reflected off the top wall and is not propagating downward. The diffracted Mach stem (D) has formed a triple point with the reflected shock (H), whereas above the incident shock (A) (not shown in the figure) has almost been eliminated. By this time, the upstream end of slip layer (C) has become completely engulfed by the vortex (F), where it follows closely with the entropy layer (G). Predictions indicate supersonic flow above the vortex layer terminating at the reflected shock (H), whereas the shock (I) continues to expand. Our numerical results have demonstrated good resolution of all flow features and are in very good agreement with those of the experiment. In Figures 6 and 7, the results of WENO5_R scheme using coarse and fine grid system and WENO5_R with anti-diffusive flux

DOI: 10.1002/fld

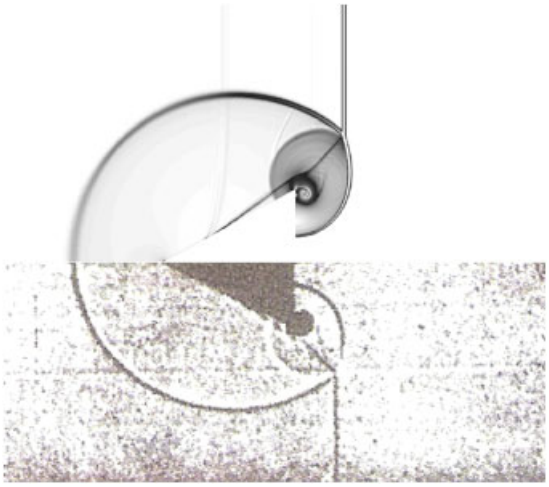

Figure 4. The $\nabla\rho$ contours using WENO5_R with anti-diffusive flux corrections scheme compared with the shadowgraph of Schardin's experiment 9 (frame 4).

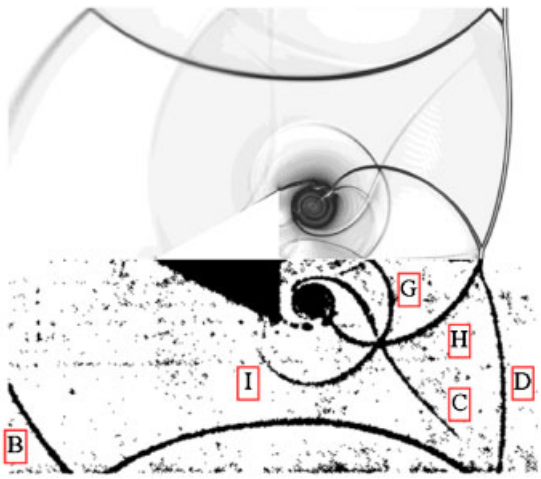

Figure 5. The $\nabla\rho$ contours using WENO5_R scheme with anti-diffusive flux corrections and a comparison with the shadowgraph of Schardin's experiment (frame 9).

corrections scheme using coarse grid system are shown, respectively, for the two different instants. By examining shock (I) and slip layer (C), the results indicate that the contact discontinuities of the WENO5_R with anti-diffusive flux correction scheme are sharpened markedly compared with the WENO5_R scheme using the same coarse grid system, similar to those of the WENO5_R scheme using fine grid system.

We note that all the WENO5 schemes give very good resolution of the flow features in every aspect. The use of anti-diffusive flux seems to reduce the spreading of the slip layer and improve

DOI: 10.1002/fld

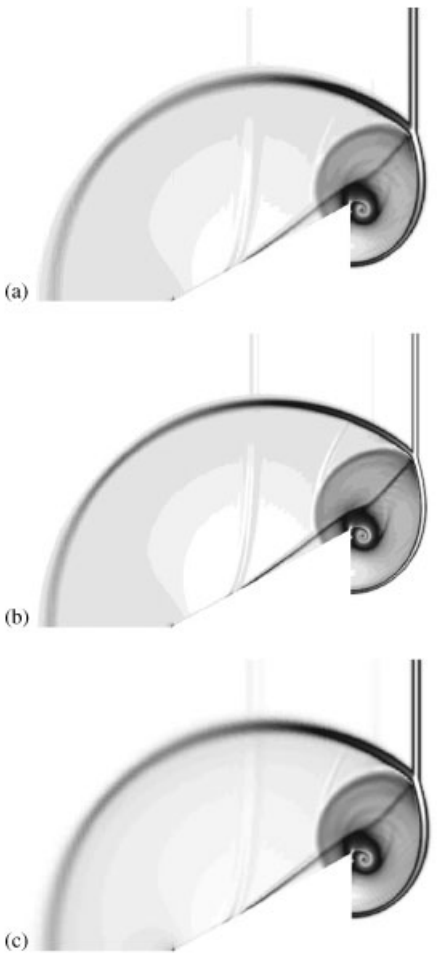

Figure 6. A comparison of $\nabla\rho$ contours at early stage: (a) WENO5_R scheme with coarse grids; (b) WENO5-R with fine grids; and (c) WENO5_R with anti-diffusive flux and coarse grids.

its resolution. The better resolution of slip layer (C) may play a more important role in viscous highly vortical flows.

6.2. Steady transonic flow over NACA 0012 airfoil

The first steady result using implicit variant WENO methods is the transonic flow over NACA 0012 airfoil at a free stream Mach number of 0.80 and with 1.25° angle of attack. For these conditions, a moderately large pocket of supersonic flow forms in the region above the upper surface, terminated by a rather strong shock, whereas a small supersonic zone terminated by a very weak shock forms below the lower surface. The calculations are performed on two 'C'-type grid systems, containing 321×49 and 193×37 cells with 241 and 145 grid points around the airfoil surface, respectively. The mesh system extends from the airfoil surface to a circular far field

DOI: 10.1002/fld

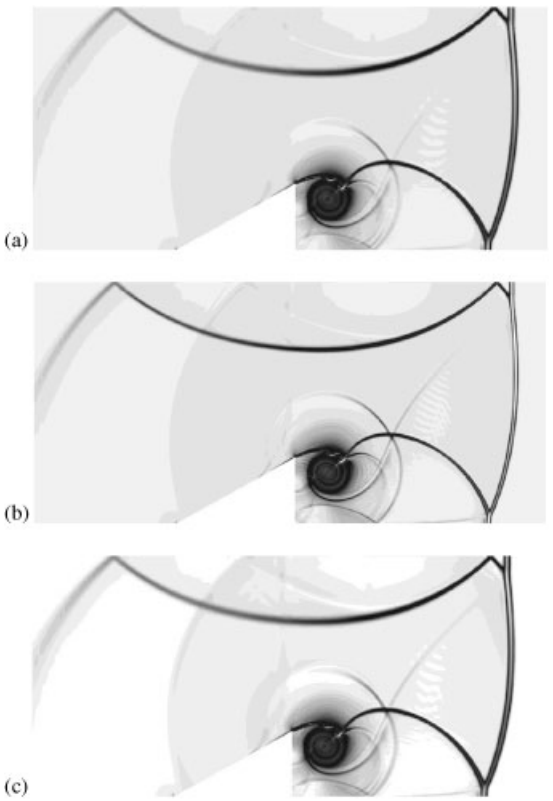

Figure 7. A comparison of $\nabla\rho$ contours at late stage: (a) WENO5_R scheme with coarse grids; (b) WENO5-R with fine grids; and (c) WENO5_R with anti-diffusive flux and coarse grids.

boundary located approximately 40 chord lengths from the airfoil. The LU-SGS implicit method is applied for time marching and the variant WENO methods can be applied to the right-hand side.

Figure 8 shows the surface pressure distributions using WENO5-R and WENO5-R with anti-diffusive flux correction schemes based on the fine and coarse grid systems, respectively. It is noted that the solutions of WENO5-R with anti-diffusive flux corrections scheme using the coarse grid system are nearly the same in comparison with that of WENO5-R using the fine grid system. Figure 9 shows a comparison of WENO5-R with anti-diffusive flux correction scheme and WENO5-LF with anti-diffusive flux correction scheme based on the same grid system; the solutions are nearly the same, except for the fact that the weak shock on the lower surface of the airfoil is slightly more smeared using the Lax–Friedrichs flux. Both these schemes can capture the shocks at the upper surface within 1–2 grid cells. Figure 10 shows the convergence histories for the variant WENO schemes using the same coarse grid system. In this case, the original WENO5-R gives the best convergence rate but the curve progresses with marked oscillations than the others. A residual of 10^{-13} can be reached in about 6000 steps using the original WENO5-R scheme. In general, all four schemes demonstrate the convergence property quite well in our implicit finite

DOI: 10.1002/fld

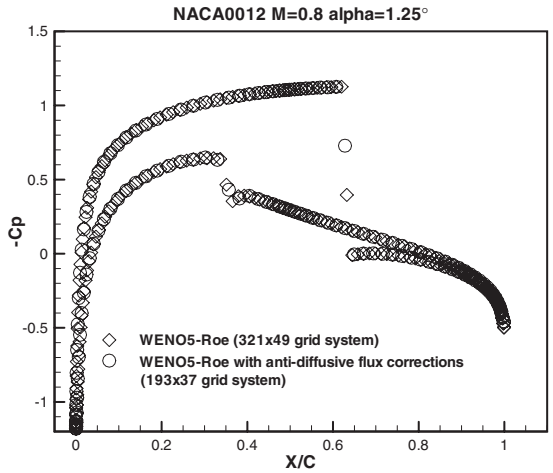

Figure 8. Surface pressure distribution of NACA 0012 airfoil. A comparison of WENO5-R and WENO5-R schemes with anti-diffusive flux corrections.

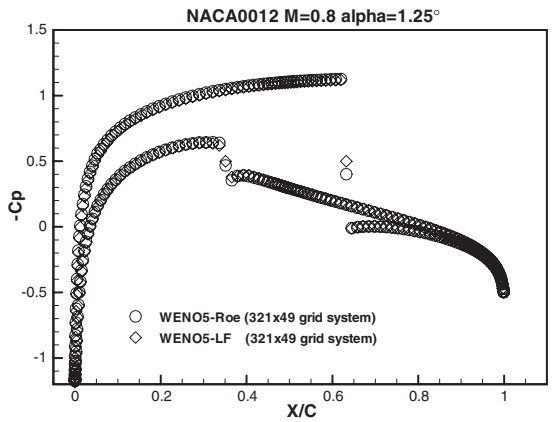

Figure 9. Surface pressure distribution of NACA 0012 airfoil. A comparison of WENO5-R and WENO5-LF schemes.

volume method. Figure 11 shows contours of constant pressure of WENO5-R with anti-diffusive flux corrections scheme. The strong shock at the upper surface and the weaker shock at the lower surface are all well resolved. A comparison of the entropy contours using WENO5-R, WENO5-R with anti-diffusive flux, mapped WENO5 and WENO5 with modified smoothness monitor is shown in Figure 12. In general, a very small amount of entropy is produced for all the WENO5 schemes (which are highly accurate) and a smaller entropy production can be observed near the trailing edge for the anti-diffusive WENO solutions. We note that indeed the effect of the anti-diffusive flux correction is to improve the resolution of contact discontinuities without sacrificing accuracy and stability of the original WENO scheme.

DOI: 10.1002/fld

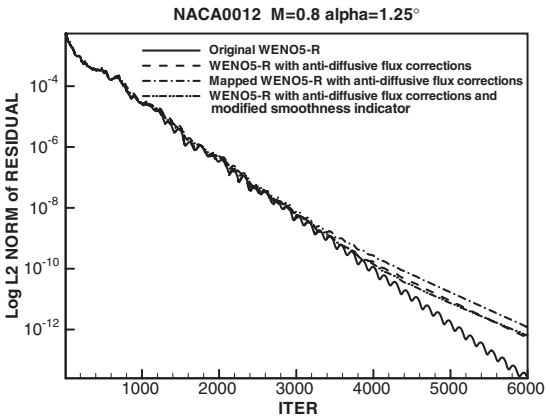

Figure 10. Convergence history of implicit variant WENO methods for NACA 0012 airfoil (193×37 grid system).

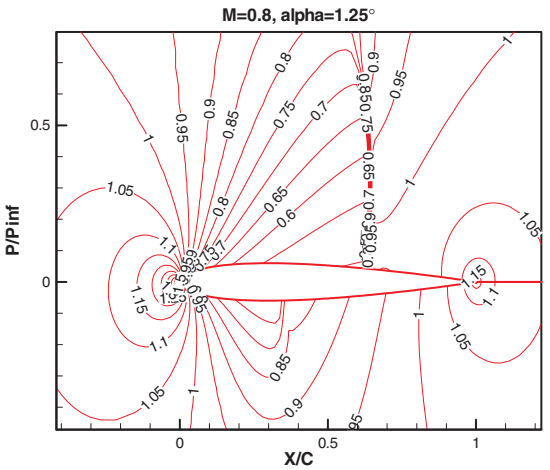

Figure 11. Pressure contours of NACA 0012 airfoil: WENO5-R scheme with anti-diffusive flux corrections.

6.3. Steady transonic flow over RAE 2822 airfoil

Lastly, we examine the steady results using implicit variant WENO methods for the inviscid transonic flow around the RAE 2822 airfoil at a free stream Mach number of 0.75 and 3.0° angle of attack. Solutions were obtained for this case on two 'C'-type meshes consisting of 161×49 and 321×49 cells with 241 and 169 grid points around the airfoil surface, respectively. The outer boundary is extending out to a radius of about 40 chords. The solutions were calculated using the same schemes as the NACA0012 test case. In Figure 13, the surface pressure coefficients of WENO5-R based on the fine grid system and WENO5-R with anti-diffusive flux correction scheme based on the coarse grid system are compared with a reference solution [25] (321×61 grids). It is noted that our calculations are in excellent agreement with the reference solution.

DOI: 10.1002/fld

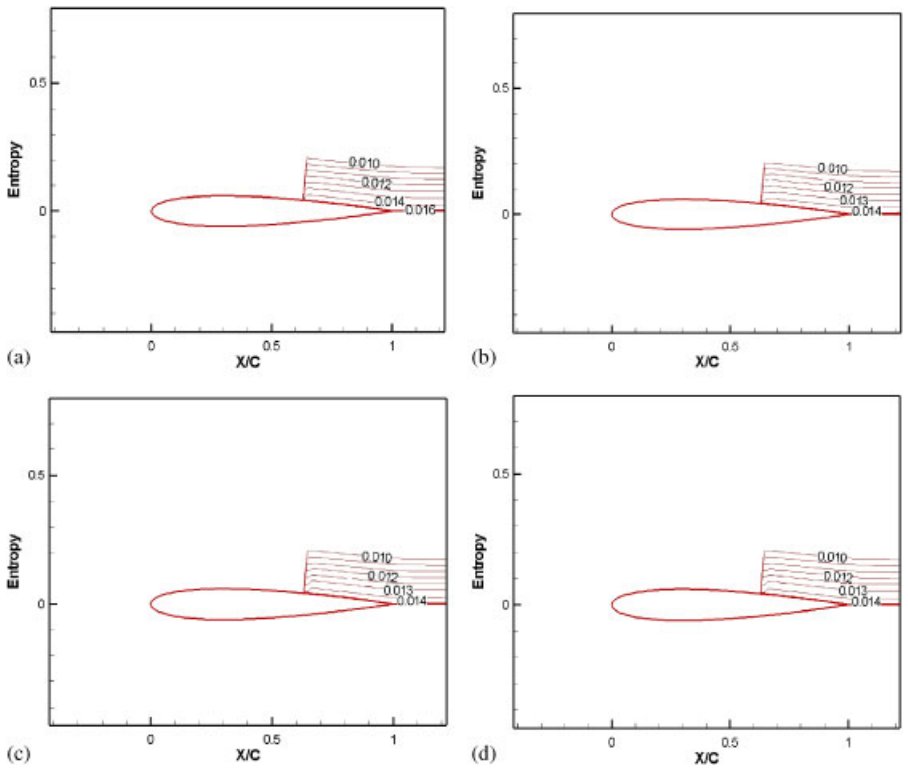

Figure 12. A comparison of entropy contours of NACA 0012 airfoil: (a) WENO5-R scheme; (b) WENO5-R with anti-diffusive flux; (c) mapped WENO5-R with anti-diffusive flux; and (d) WENO5-R with modified smoothness monitor and anti-diffusive flux.

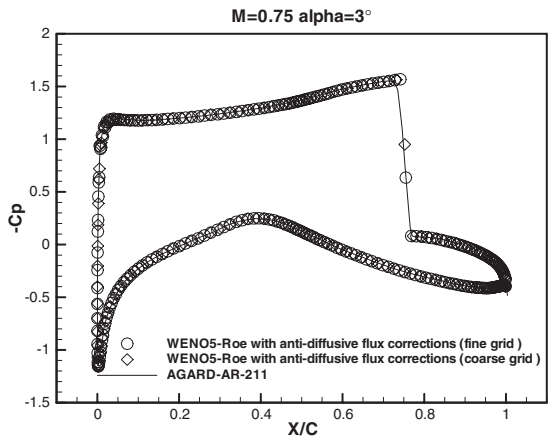

Figure 13. A comparison of surface pressure distributions of RAE 2822 airfoil.

DOI: 10.1002/fld

Figure 14 shows the convergence histories for various schemes using the same fine grid system. Again, the WENO5-R scheme gives the best convergence rate and the curve progresses with more notable oscillations than the others. A residual of 10^{-12} can be obtained in about 6000 steps using WENO5-R scheme for this case. In general, all four schemes demonstrate the convergence property quite well in our implicit finite volume method. The Mach contours for WENO5-R with anti-diffusive flux correction schemes are shown in Figure 15. Very good resolution of the flowfields can be achieved. A comparison of the entropy contours using WENO5-R, WENO5-R-AD, mapped WENO5-R-AD, and WENO5 with modified smoothness monitor and anti-diffusive flux is given in Figure 16. It is noted that a noticeabledifference in entropy production can be observed near the trailing edge for the anti-diffusive WENO methods. Again, the main function of the anti-diffusive

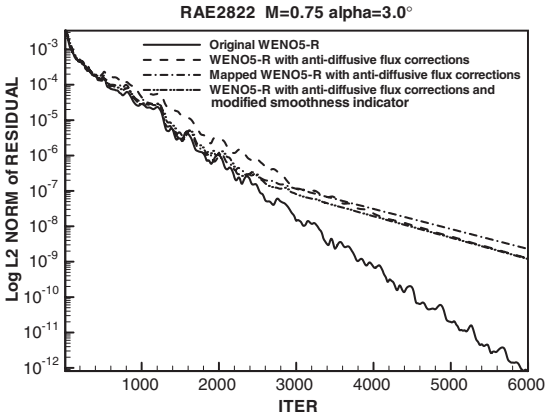

Figure 14. Convergence history of implicit variant WENO methods for RAE2822 airfoil (321×49 grid system).

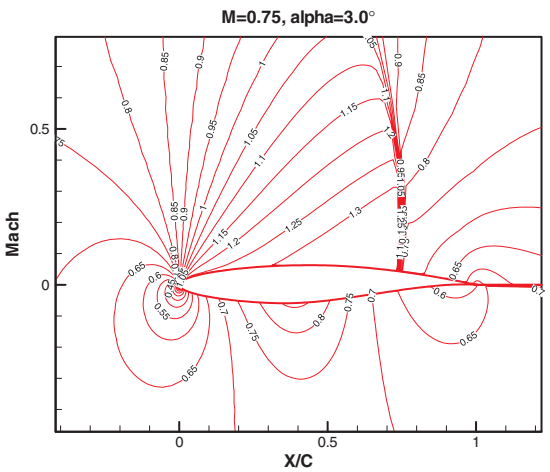

Figure 15. Mach contours of RAE2822 airfoil using WENO5-R scheme with anti-diffusive flux.

DOI: 10.1002/fld

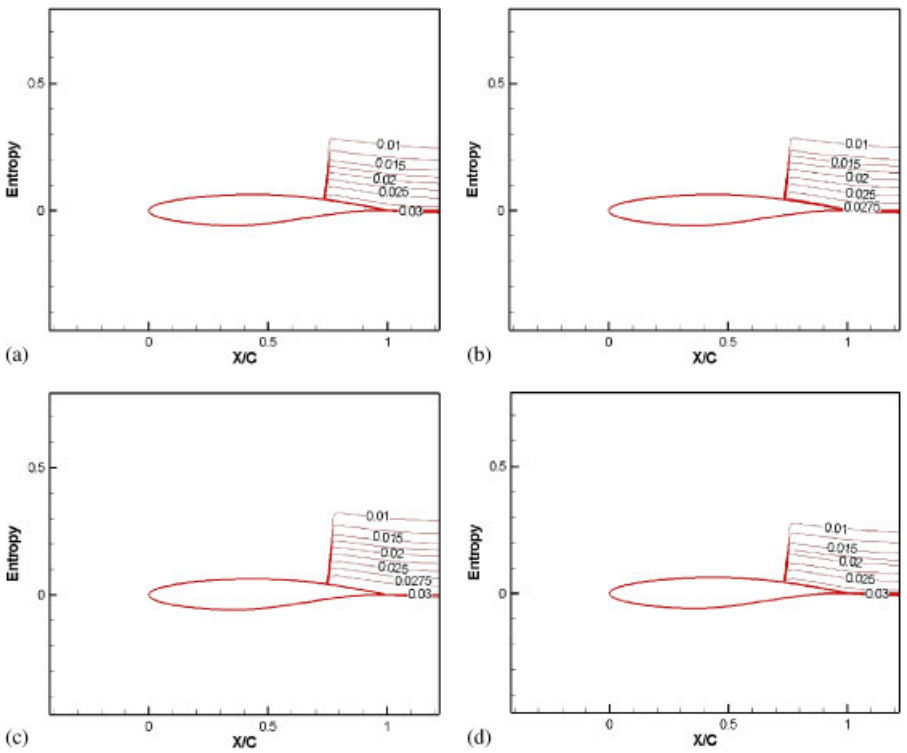

Figure 16. A comparison of entropy contours of RAE 2822 airfoil: (a) WENO5-R scheme; (b) WENO5-R with anti-diffusive flux; (c) mapped WENO5-R with anti-diffusive flux; and (d) WENO5-R with modified smoothness monitor and anti-diffusive flux.

flux corrections is indeed to improve the resolution of contact discontinuities without sacrificing accuracy and stability of the original WENO scheme.

7. CONCLUDING REMARKS

The explicit TVD Runge–Kutta high-order WENO schemes with anti-diffusive flux corrections of Xu and Shu [16] have been adopted to a finite volume WENO method with a new numerical flux which consists of a first-order method and a high-order part. This new flux formulation allows a more flexible choice of first-order positive entropy-satisfying scheme. Also, a class of efficient and accurate Euler solvers using implicit LU-SGS time stepping and high-order WENO spatial operator with variant WENO methods such as anti-diffusive flux corrections, mapped WENO, or modified smoothness indicator has been developed. Numerical experiments with these explicit and implicit variant WENO schemes to two-dimensional inviscid compressible flows have been carried out. Computations of unsteady shock wave reflection over a wedge in a shock tube involving complex shock diffraction patterns indicate that all the variant WENO schemes can capture the flow features excellently and in good agreement with the experimental results of Schardin. Moderate improvement of slip layer can be observed when anti-diffusive flux correction

DOI: 10.1002/fld

is employed. Calculations of steady transonic flows over NACA 0012 and RAE 2822 airfoils have been carried out to validate and illustrate the implicit methods. From the present results it is noted that the use of WENO spatial operator for the numerical fluxes not only enhances the accuracy but also improves the convergence rate for steady-state computation as compared with those using the ENO counterpart. *Among the three schemes* (*WENO5-LF*, *WENO5-R*, *and WENO5-R with anti-diffusive flux corrections*) *tested*, *WENO5-R with anti-diffusive flux corrections scheme* gives the best performance for these two transonic airfoil flows. Also various aspects are tested for the variant WENO schemes, including the original WENO schemes, the WENO scheme with anti-diffusive flux corrections, the mapped WENO scheme with anti-diffusive flux corrections, and finally the WENO scheme with both anti-diffusive flux corrections and modified smoothness indicator. By using the WENO scheme with anti-diffusive flux corrections, the present solutions indicate that good convergence rate can be achieved and high-order accuracy is maintained and contact discontinuities are sharpened compared with the original WENO schemes on the same meshes. It is also noted that the use of anti-diffusive flux can lead to the slowdown of the convergence rate of implicit methods. From the entropy contours of the airfoil calculations, we observe that indeed the main effect of the anti-diffusive flux correction is to improve the resolution of contact discontinuities (lower entropy production) without sacrificing accuracy and stability of the original WENO scheme. This property of better resolution of slip layer will have more important impact and consequence on viscous highly vortical flows. A further test of the performance for the implicit WENO-LF and WENO-R schemes with anti-diffusive flux correction for vortical viscous flows is currently being investigated and will be reported separately.

ACKNOWLEDGEMENTS

This work was done under the auspice of National Science Council, Taiwan, through Grant NSC-95-2212-E002-055. We thank Yeu-Ching Perng, Shih-Chang Yang, Horng-Tsair Lee, and Herng Lin of Chung-Shan Institute of Science and Technology for many useful discussions.

REFERENCES

1. Harten A, Engquist B, Osher S, Chakravarthy S. Uniformly high-order accurate nonoscillatory scheme. III. *Journal of Computational Physics* 1987; **71**:231–303.
2. Shu CW, Osher S. Efficient implementation of nonoscillatory shock capturing schemes. *Journal of Computational Physics* 1988; **77**:439–471.
3. Shu CW, Osher S. Efficient implementation of nonoscillatory shock capturing schemes. II. *Journal of Computational Physics* 1989; **83**:32–78.
4. Shu CW. Essentially non-oscillatory and weighted essentially non-oscillatory schemes for hyperbolic conservation laws. In *Advanced Numerical Approximation of Nonlinear Hyperbolic Equations*, Cockburn B, Johnson C, Shu CW, Tadmor E, Quarteroni A (eds). Lecture Notes in Mathematics, vol. 1697. Springer: Berlin, 1998; 325–432.
5. Yee HC, Harten A. Implicit TVD schemes for hyperbolic conservation laws in curvilinear coordinates. *AIAA Journal* 1987; **25**:266–274.
6. Harten A. A high resolution scheme for the computation of weak solutions of hyperbolic conservation laws. *Journal of Computational Physics* 1983; **49**:357–393.
7. Liu XD, Osher S, Chan T. Weighted essentially nonoscillatory schemes. *Journal of Computational Physics* 1994; **115**:200–212.
8. Jiang GS, Shu CW. Efficient implementation of weighted ENO schemes. *Journal of Computational Physics* 1996; **126**:202–228.
9. Atkins H. High-order ENO methods for the unsteady compressible Navier–Stokes equations. *AIAA Paper 91-1557*, 1991.

DOI: 10.1002/fld

10. Perng YC, Yen RH, Yang JY. Implicit weighted ENO schemes for the Euler equations. *Computational Fluid Dynamics Journal* 1999; **8**:216–227.
11. Yang JY, Perng YC, Yen RH. Implicit weighted ENO schemes for the three-dimensional compressible Navier–Stokes equations. *AIAA Journal* 1998; **38**:464–487.
12. Yang JY, Yang SC, Chen YN, Hsu CA. Implicit weighted ENO schemes for the three-dimensional incompressible Navier–Stokes equations. *Journal of Computational Physics* 1998; **146**:464–487.
13. Chorin AJ. A numerical method for solving incompressible viscous flow problems. *Journal of Computational Physics* 1967; **2**:12–24.
14. Despres B, Lagoutiere F. Contact discontinuity capturing schemes for linear advection, compressible gas dynamic. *Journal of Scientific Computing* 2001; **16**:479–524.
15. Bouchut F. An antidiffusive entropy scheme for monotone scalar conservation law. *Journal of Scientific Computing* 2004; **21**:1–30.
16. Xu Z, Shu CW. Anti-diffusive flux corrections for high order finite difference WENO scheme. *Journal of Computational Physics* 2005; **205**:458–485.
17. Henrick AK, Aslam TD, Powers JM. Mapped weighted essentially non-oscillatory schemes. *Journal of Computational Physics* 2005; **207**:542–567.
18. Zhang SH, Shu CW. A new smoothness indicator for the WENO schemes and its effect on the convergence to steady state solutions. *Journal of Scientific Computing* 2007; **31**:273–305.
19. Lax PD. Weak solution of nonlinear hyperbolic equations and their numerical computation. *Communications on Pure and Applied Mathematics* 1954; **7**:159–193.
20. Roe P. Approximate Riemann solvers, parameter vectors and difference schemes. *Journal of Computational Physics* 1981; **43**:357–372.
21. Yoon S, Jameson A. Lower–upper symmetric-Gauss–Seidel method for the Euler and Navier–Stokes equations. *AIAA Journal* 1988; **26**:1025–1026.
22. Jameson A, Yoon S. Lower–upper implicit schemes with multiple grids for the Euler equations. *AIAA Journal* 1987; **25**:929–935.
23. Dadone A, Grossman B. Surface boundary conditions for the numerical solution of the Euler equations. *AIAA Journal* 1994; **32**:285–293.
24. Schardin H. High frequency cinematography in the shock tube. *Journal of Photographic Science* 1957; **5**:19–26.
25. Viviand H. Numerical solutions of two dimensional reference test cases. *AGARD Advisory Report AGARD-AR-211*: *Test Cases for Inviscid Flow Field Methods*, Chapter 6, 1985; 6.52–6.58.

DOI: 10.1002/fld